Bending of magnetic filaments under a magnetic field

Valera P. Shcherbakov
Geophysical Observatory "Borok" of the Russian Academy of Science, Borok Yaroslavskaja oblast, 151742, Russia

Michael Winklhofer*
Department of Earth and Environmental Science—Geophysics Section, Ludwig-Maximilians-Universität, Theresienstrasse 41, D-80333 München, Germany†

(Received 24 May 2004; published 27 December 2004)

Magnetic beads and superparamagnetic (SP) colloid particles have successfully been employed for micromechanical manipulation of soft material, *in situ* probing of elastic properties, and design of smart materials (ferrogels). Here we derive analytical expressions for the equilibrium shape of magnetic fibers, considering two end-member cases, (a) SP or single-domain particles concentrated at the free end of cantilevered rods or tubes, and (b) filaments consisting of SP particles, with this case being mathematically equivalent to tubes containing SP particles. Our analysis yields also metastable equilibrium states (MES's), which only exist above a critical filament length, but become more stable with increasing magnetic field. The MES's for case (a) are, like the ground state, circular arcs, but more strongly bent. The multiform MES's in case (b), which comprise hairpin, sinuous, or even closed shapes, have recently been observed in experiments, too. We also study the effect of gravity on the balance between bending and magnetic energy, which leads to curves with inflection point if the influence of gravity is stronger than that of the magnetic field. Because of their simple experimental realization, case (a) magnetic filaments are deemed highly suitable for micromechanical experiments on long chains of polymer molecules. Another potential application of cantilevered magnetic filaments with magnetic material attached to the free end is in scanning probe microscopes. Because the magnetic field due to the magnetic tip is comparatively weak, the magnetization structure of the sample to be investigated would not be affected by the probe. Thus, for the examination of magnetically soft materials, probes in the form of magnetic filaments may hold advantages over tips usually employed in magnetic force microscopy.

DOI: 10.1103/PhysRevE.70.061803 PACS number(s): 82.35.Np, 46.25.Hf, 46.70.Hg, 82.70.Dd

I. INTRODUCTION

Allowing for noninvasive, precise application of point torques and point forces to soft materials, magnetic beads have been used in micromechanical experiments to measure stress-strain curves of biological materials ranging from single DNA molecules [1] and actin bundles [2] up to stretch receptors of living cells [3]. Nevertheless, the precise determination of elastic moduli using the magnetic bead method requires a sound mathematical framework to describe the magnetoelastic response of the system. We here derive analytical expressions for the equilibrium shape of magnetic filaments under a magnetic field, which can be used to determine the bending rigidity of the filaments. We first examine the mathematically simpler case of superparamagnetic (SP) or permanent-magnetic particles bound to the free end of an otherwise nonmagnetic cantilevered filament and analyze stable and metastable equilibrium states (MES's). We will also reconsider the case of a filament with magnetic material distributed along the filament, a system recently designed for a micromechanical approach to probe elastic parameters at molecular scale [4–6]. Goubault *et al.* [4] produced long flexible filaments from monodisperse superparamagnetic colloid particles connected through molecular linkers, and were able to determine the bending rigidity of the linkers from the magnetoelastic response of the filaments. We take their mathematical approach one step further and derive analytical expressions for the static equilibrium shape of magnetic filaments for different scenarios. The dynamics of such a system in a rotating magnetic field has lately been investigated [7,8]. The magnetoelastic behavior of the single-domain equivalent to SP filaments, which in nature occurs in the form of chains of magnetosomes in magnetotactic bacteria [9], was examined earlier [10]. In the last section, we loosen the constraint of bending in the horizontal plane and present a formalism to include the influence of gravity.

II. MATHEMATICAL ANALYSIS

We first consider the case of a fiber with magnetic material concentrated at the free end. The fixed end of the fiber defines the origin of the (x,y) coordinate system (Fig. 1). In the undeformed state, the fiber is parallel to x. The external magnetic field is applied horizontally at an angle D (declination). In the deformed state, l is the curvilinear abscissa along the fiber. The shape of the deformed fiber may be described by the angle $\psi(l)$ between x and the local tangent $d\boldsymbol{l}$ of the bent fiber; at the fixed end, $\psi(l=0)=\psi_0=0$. We chose a continuum-mechanics approach to calculate the elastic energy of the fiber: According to the Kirchhoff model of a nonstretchable elastic rod, the elastic energy stored in a bent rod is given by $(1/2)EI\int dl/R_c^2$, where $1/R_c$ is the local

*Electronic address: MICHAELW@LMU.DE
†URL: http://www.geophysik.uni-muenchen.de/ ~michael

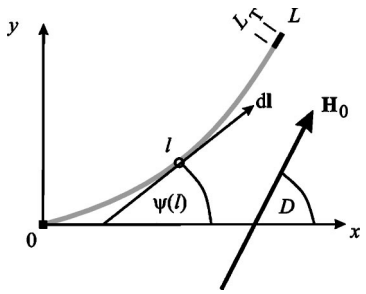

FIG. 1. Coordinate system. The deformation of the fiber (gray) is described by the angle $\psi(l)$. The local tangent $d\boldsymbol{l}$ is given by $(\cos\psi,\sin\psi)dl$. The external magnetic field $\mathbf{H}_0$ is homogeneous and applied horiztonally. The magnetic material (black) is bound to the tip of the fiber. The length of the magnetic tip, L_T, is much smaller than the total length of the fiber, L.

curvature, E is Young's modulus, and I is the area moment of inertia of the rod. A filament can be regarded as a long cylinder with $I=S^2/\pi$ constant over its length. With $\dot{x}=\cos\psi$ and $\dot{y}=\sin\psi$, where the overdot denotes differentiation with respect to the curve parameter l, $1/R_\mathrm{c}$ is given by $\dot{\psi}$.

A. Superparamagnetic tip

The tip of the fiber (length of tip, $L_\mathrm{T} \ll$ length of fiber, L), has superparamagnetic material attached to it with effective susceptibility χ. Its total magnetic energy is

$$W_\mathrm{SP} = -\frac{1}{2}\chi^2 H_0^2 \left(\frac{\sin^2(D-\psi_1)}{1+\chi N_1} + \frac{\cos^2(D-\psi_1)}{1+\chi N_2} \right) S L_\mathrm{T}, \quad (1)$$

where $\psi_1=\psi(l=L)$, S is the area of the cross section, and N_1 and N_2 are the demagnetizing factors along the short and long axes of the SP tip, respectively. In order for a SP system to produce a torque, it has to have a shape anisotropy, that is, $N_1 \neq N_2$. Assuming that $L_\mathrm{T} \gg \sqrt{S}$, then $N_1 \approx 0$, $N_2 \approx 4\pi$, and Eq. (1) becomes

$$W_\mathrm{SP}(\psi_1) = \underbrace{\frac{2\pi\chi^3 H_0^2 S L_\mathrm{T}}{1+4\pi\chi}}_{W_\mathrm{SP}^0} \sin^2(D-\psi_1). \quad (2)$$

Thus, the SP system produces a torque of magnitude

$$T_\mathrm{SP} = -\frac{dW_\mathrm{SP}}{d\psi_1} = -W_\mathrm{SP}^0 \sin 2(D-\psi_1), \quad (3)$$

which gives rise to a bending torque of magnitude $T_\mathrm{b}=EI/R_\mathrm{c}$.

We determine the equilibrium deformation of the fiber by minimizing its free energy functional,

$$\omega_\mathrm{tot} = \sin^2(D-\psi_1) + \frac{l_0}{2}\int_0^L \left(\frac{d\psi}{dl}\right)^2 dl, \quad (4)$$

where l_0, the characteristic length scale of the system, is defined as the ratio of the structural rigidity EI to the characteristic magnetic energy W_SP^0,

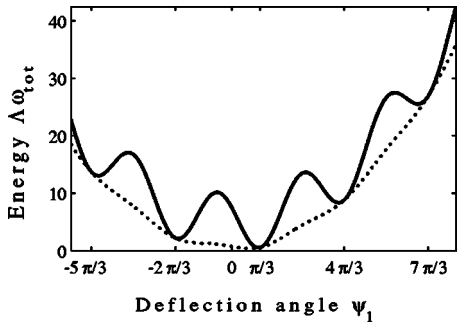

FIG. 2. Total energy $\Lambda\omega_\mathrm{tot}$ as a function of ψ_1 calculated according to Eq. (10) for $\Lambda=1$ (dotted) and $\Lambda=10$ (solid). The energy ω_tot is multiplied by Λ to allow for better comparison of the two graphs. The magnetic field angle D is $\pi/3$. For $\Lambda=1$, the position of the minimum is at $\psi_1=0.676$, but shifts to $\psi_1=0.997$ for $\Lambda=10$.

$$l_0^\mathrm{SP} = \frac{(1+4\pi\chi)EI}{2\pi\chi^3 H_0^2 S L_\mathrm{T}}. \quad (5)$$

This magnetoelastic length of the fiber, l_0^SP, can be used to express the total energy (4) in terms of dimensionless variables,

$$\omega_\mathrm{tot} = \sin^2(D-\psi_1) + \int_0^\Lambda \frac{1}{2}\left(\frac{d\psi}{d\lambda}\right)^2 d\lambda, \quad (6)$$

where $\Lambda = L/l_0^\mathrm{SP}$ and $d\lambda = dl/l_0^\mathrm{SP}$.

Variation of the total energy (6) furnishes the Euler equation,

$$\delta\omega_\mathrm{tot} = 0 \Leftrightarrow \frac{d^2\psi}{d\lambda^2} = 0 \Rightarrow \frac{d\psi}{d\lambda} = k, \quad (7)$$

that is, the curvature $\dot{\psi}$ is constant and the equilibrium shape of the fiber is a circular arc. The constant of integration k can be determined from the boundary conditions. The magnetic point torque acting upon the free end produces a jump in the bending torque at the free end, that is,

$$k = \left(\frac{d\psi}{d\lambda}\right)_{\lambda=\Lambda} = \sin 2(D-\psi_1), \quad (8)$$

Equations (7) and (8) can be combined in the form

$$\psi(\lambda) = \lambda \sin 2(D-\psi_1) \quad (9)$$

where ψ_1 can be determined from minimizing the total energy (6), which because of the uniform curvature (7) simplifies to

$$\omega_\mathrm{tot} = \sin^2(D-\psi_1) + \frac{\psi_1^2}{2\Lambda}. \quad (10)$$

Figure 2 shows ω_tot as a function of ψ_1. For $\Lambda=1$, magnetic energy and bending energy are in a subtle balance and there is only one minimum ($\psi_1=0.676$), which is not very pronounced either. For $\Lambda=10$, the first and most favorable minimum has deepened and shifted toward the asymptotic value of $\psi_{1,\infty}=D$, which means perfect alignment of the SP tip with the external magnetic field. In addition to the ground state, there exist metastable equilibrium states as well, which

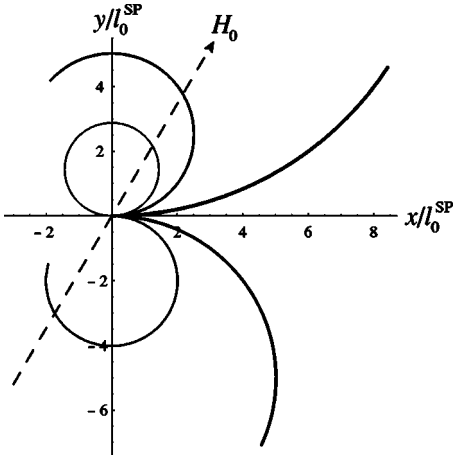

FIG. 3. Equilibrium shapes corresponding to the five energy minima in Fig. 2 at $\psi_1=0.997$, $\psi_{1,\alpha-}=-1.994$, $\psi_{1,\alpha+}=3.983$, $\psi_{1,\beta-}=-4.976$, and $\psi_{1,\beta+}=6.946$. The straight dashed line represents the magnetic field vector. The relative thickness of the curves is an inverse measure of the energy of the corresponding states. Parameters: $\Lambda=10$, $D=\pi/3$.

are depicted in Fig. 3. Which one of the MES's is realized depends on the initial curvature of the rod.

To calculate Λ_{crit}, the critical value of Λ above which MES's can exist, we minimize (10) with respect to ψ_1 and obtain $\Lambda^*=\psi_1/\sin 2(D-\psi_1)$ for $\psi_1>0$. $\Lambda_{\mathrm{crit},i+}$ with $i\in\{\alpha,\beta\}=\{1,2\}$ is the minimum on the $(i+1)$th positive branch of Λ^*. Our numerical analysis yields $\Lambda_{\mathrm{crit},\alpha+}\cong 2.31+D$ and $\Lambda_{\mathrm{crit},\beta+}\cong 5.48+D$ for the two MES's with $\psi_1>0$ $(D<\pi/2)$. The corresponding bending angles are $\psi_{1,\alpha+}\cong 2.25+D$ and $\psi_{1,\beta+}\cong 5.45+D$, respectively, that is, the orientation of the tip is lagging behind the ideal alignment angle of $\pi+D$ and $2\pi+D$, respectively. As Λ increases, the magnetic energy more and more dominates the total energy and the tip becomes increasingly aligned with the field. This can also be understood in terms of (5), according to which $\Lambda\propto H_0^2$ for a rod of given length L. A good alignment (95% criterion) is achieved for $\Lambda\approx 10$. The threshold length for MES's with $\psi_1<0$, $\Lambda_{\mathrm{crit},i-}$, is obtained as the minimum of the ith branch of $\Lambda^*=-\psi_1/\sin 2(D+\psi_1)$, leading to $\Lambda_{\mathrm{crit},\alpha-}\cong 2.31-D$ and $\Lambda_{\mathrm{crit},\beta-}\cong 5.48-D$.

B. Permanent-magnetic tip (i.e., $M_r \gg \chi^2 H_0$)

In the case of a permanent-magnetic material bound to the free end of the fiber, the magnetic energy is

$$W_{\mathrm{SD}}(\psi_1) = -M_r H_0 \cos(D-\psi_1) S L_{\mathrm{T}}, \tag{11}$$

where we assume that the vector of the remanent magnetization $\mathbf{M}_r$ is parallel to the tangent $d\boldsymbol{l}$ of the tip and the external field H_0 is smaller than the coercive force H_c. From the magnetic point of view, single-domain (SD) particles are preferable than pseudo-single-domain or multidomain particles as they have higher H_c and do not show nonlinear magnetization behavior, that is, the magnetic remanence is always equal to the saturation magnetization. In that case, the magnetostatic self-energy is constant and can be neglected. The

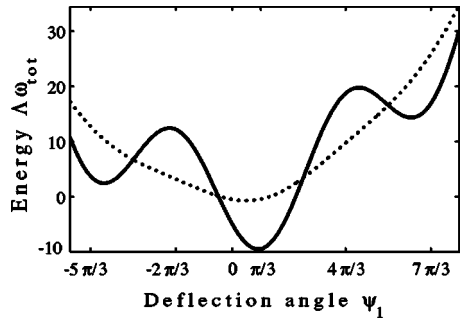

FIG. 4. Total energy $\Lambda\omega_{\mathrm{tot}}$ for a permanent-magnetic tip as a function of ψ_1 for $\Lambda=1$ (dotted) and $\Lambda=10$ (solid). The magnetic field angle D is $\pi/3$. The position of the minimum is at $\psi_1=0.511$ for $\Lambda=1$. For $\Lambda=10$, the three minima are located at $\psi_1=0.952$, $\psi_1=-4.74$, and $\psi_1=6.61$.

dimensionless length here is given by $l_0^{\mathrm{SD}}=EI/(M_r H_0 S L_{\mathrm{T}})$. The Euler equation for the SP case carries over unchanged and we simply have to adjust the boundary condition to find the new constant of integration, that is,

$$k=\sin(D-\psi_1).$$

Compared to Eq. (8), the dimensionless magnetic torque produced by a SD tip is just half as much as that due to a SP tip, and, consequently, SP tips will give better alignment with the external field than SD tips provided the filaments are soft enough. This is demonstrated by comparing Fig. 4 with Fig. 2. The positions of the minima in the SP case are nearer to perfect alignment than in the SD case. $\Lambda^{\mathrm{SP}}\sim 10$ and $\Lambda^{\mathrm{SD}}\sim 19$ correspond to 95% alignment of the tip with the magnetic field, respectively. In absolute units, however, $l_0^{\mathrm{SD}}/l_0^{\mathrm{SP}}\sim\chi^3 H_0/M_{\mathrm{r}}$; thus for a given length L, $\Lambda^{\mathrm{SD}}>\Lambda^{\mathrm{SP}}$.

In contrast to the SP case, the antiparallel alignment of the tip for $\psi_1>0$ is forbidden in the SD case, and the first MES—the more strongly curved arc—can develop only for $\psi_1<0$, here at $\psi_1=-4.74$ (Fig. 4), with a critical length of $\Lambda_{\mathrm{crit}}=4.66-1.1D$. For the spiral shape ($\psi_1=6.61$), we find $\Lambda_{\mathrm{crit}}=4.61+D$. The corresponding shapes are depicted in Fig. 5.

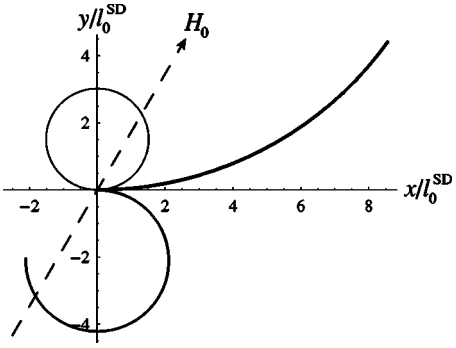

FIG. 5. Equilibrium shapes corresponding to the three energy minima in Fig. 4 ($\Lambda=10, D=\pi/3$). The straight dashed line represents the magnetic field vector. The relative thickness of the lines is an inverse measure of the energy of the corresponding states.

C. Magnetic material distributed over fiber

We next consider the case where the magnetic material is distributed uniformly over the whole length of the fiber, as in the technically produced filaments composed of SP colloid particles connected by molecular linkers [4–8]. We now derive analytical expressions for the magnetoelastic equilibrium shape of the one-dimensional magnetic elastomer. For our analysis, it is sufficient to include the magnetic energy into the Kirchhoff model of elastic rods; readers who are interested in the complete continuum theory for magnetic elastomers (ferrogels) are referred to recent work by Refs. [11] and [12]. The magnetic energy of each linear element dl is

$$dW_{\mathrm{mag}} = \underbrace{\frac{2\pi\chi^3 H_0^2 S}{1+4\pi\chi}}_{dW_{\mathrm{SP}}^0} \sin^2[D-\psi(l)]dl.$$

The total free energy functional now is given by

$$W = \int_0^L \left\{ \frac{E^* I}{2}\left(\frac{d\psi}{dl}\right)^2 + dW_{\mathrm{SP}}^0 \sin^2(D-\psi)\right\} dl, \quad (12)$$

where E^* is the effective Young's modulus of the magnetoelastic material, which theoretically depends on the magnetic field strength [13]. Departures from linear elasticity have been observed in magnetorheological elastomers [14] (rubber with SP colloid particles) under a magnetic field of 20 kOe [15]. We introduce the characteristic length scale l_0, defined by

$$l_0 = \sqrt{\frac{(1+4\pi\chi)E^* I}{4\pi\chi^3 H^2 S}},$$

to recast Eq. (12) in dimensionless form,

$$\omega_{\mathrm{SP}} = \int_0^\Lambda \left\{ \left(\frac{d\psi}{d\lambda}\right)^2 + \sin^2(D-\psi)\right\} d\lambda. \quad (13)$$

We substitute $\phi = D-\psi$, where ϕ is the angle between $\mathbf{H}_0$ and $d\mathbf{l}$, and get the corresponding Euler equation as

$$2\frac{d^2\phi}{d\lambda^2} = \sin 2\phi, \quad (14)$$

with the boundary conditions

$$\phi(0) = \phi_0 = D - \psi_0 \quad \text{and} \quad \left(\frac{d\phi}{d\Lambda}\right)_{\lambda=\Lambda} = 0. \quad (15)$$

Multiplication of Eq. (14) by $d\phi/d\lambda$ and integration yields

$$\left(\frac{d\phi}{d\lambda}\right)^2 = \sin^2\phi - \sin^2\phi_1. \quad (16)$$

It is interesting to note that Eq. (16) is exactly the equation of a Bloch wall derived by Ref. [16], except for the different boundary conditions, which in the case of an infinite crystal are $\phi_0 = \phi(x=-\infty) = 0$ and $\phi_1 = \phi(x=\infty) = \pi$. From Eq. (16), we get $\lambda(\phi)$ by separation of variables:

$$\Lambda - \lambda = \int_\phi^{\phi_1} \frac{d\tilde{\phi}}{\sqrt{\cos^2\phi_1 - \cos^2\tilde{\phi}}} \quad (17)$$

$$= \int_{\phi+\pi/2}^{\phi_1+\pi/2} \frac{d\theta}{\sqrt{1-\sin^2\theta/\cos^2\phi_1}}. \quad (18)$$

Using elliptic integrals, we finally obtain

$$\Lambda - \lambda = K(\cos^2\phi_1) - F\left(\arcsin\frac{\cos\phi}{\cos\phi_1}, \cos^2\phi_1\right), \quad (19)$$

where

$$F(\phi, m<1) = \int_0^\phi \frac{d\theta}{\sqrt{1-m\sin^2\theta}}$$

is the incomplete elliptic integral of the first kind, and $K(m<1) = F(\pi/2, m)$ is the complete elliptic integral of the first kind. In our case, the parameter $m>1$; therefore we made use of $F(\phi, m>1) = m^{-1/2}F(\beta, m^{-1})$ with $\sin\beta = m^{1/2}\sin\phi$ (see Eq. 17.4.15 in Ref. [17]). We prefer using the parameter m instead of the modulus k with $m=k^2$ to allow for compatibility with mathematical computation software. Equation (19) can be solved for ϕ by applying the Jacobian elliptic function $\mathrm{sn}[F(\phi,m)|m] = \sin(\phi)$:

$$\phi(\lambda) = \arccos\{(\cos\phi_1)\mathrm{sn}[K(\cos^2\phi_1) + \lambda - \Lambda|\cos^2\phi_1]\}, \quad (20)$$

where ϕ_1 has first to be determined numerically from the constraint of constant length, that is,

$$\Lambda = K(\cos^2\phi_1) - F\left(\arcsin\frac{\cos\phi_0}{\cos\phi_1}, \cos^2\phi_1\right). \quad (21)$$

The shape of the fiber can be calculated using Eq. (A1) in the Appendix.

For the example $\Lambda = 2$, $\phi_0 = \pi/3$, $D=0$, the angle ϕ_1 computed from Eq. (21) amounts to 0.32; the corresponding shape of the rod is represented by the dotted line in Fig. 6. Evidently, a short fiber is too stiff to align its tip into the magnetic field. More deformation scenarios can be obtained by starting from a symmetrical solution $\cos\phi_1 = -\cos\phi_0$, for which Eq. (20) simplifies to

$$\Lambda = 2K(\cos^2\phi_1), \quad (22)$$

from which the minimum length $\Lambda_{\mathrm{min}} = \pi$ can be determined above which symmetrical solutions are possible. Two examples of symmetric solutions $\phi_1 = \pi - \phi_0$ (hairpins) are represented by the dashed lines in Fig. 6. In addition to the hairpin shape, we find solutions with closed (O shape) and sinuous shape (S shape), which can be constructed from the hairpin solution by symmetry considerations. Rigorously calculated O- and S-shaped solutions are shown in Fig. 6.

It is interesting to compare our results with the ones obtained by Refs. [4] and [8], who in their experiments on flexible SP filaments observed hairpin and sinuous shapes, too. The filaments in Ref. [4] were made of SP colloids with molecular linkers in the gap between two adjacent colloid particles. Their experiments were designed so as to measure

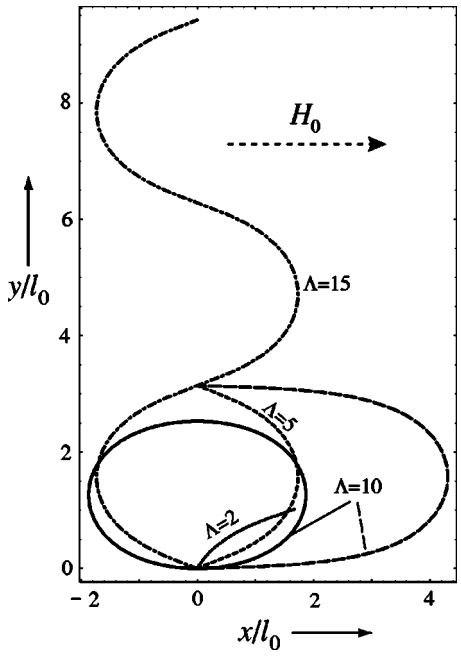

FIG. 6. Various equilibrium shapes $y(x)$ of a magnetic fiber (magnetic material distributed over the whole length of the fiber) from Eq. (A1). The magnetic field is parallel to the x axis ($D=0$). Line styles: $\Lambda=2$, $\phi_0=\pi/3$, $\phi_1=0.32$ (dot); $\Lambda=5$, $\phi_0=\pi/9$, $\phi_1=\pi-\phi_0$ (short dash); $\Lambda=10$, $\phi_0=0.027$, $\phi_1=\pi-\phi_0$ (long dash); $\Lambda=10$, $\phi_0=0$, $\phi_1=2\pi$ (solid); $\Lambda=15$, $\phi_0=\pi-\pi/9$, $\phi_1=\pi/9$ (dash dot). The hairpin shape exists for $\Lambda>\pi$. The sinuous shape has the nodal points at $x=n\pi$, $n\in\mathbb{N}_0$.

the bending rigidity of different molecular linkers from the magnetic field dependence of the filament curvature. Their magnetic filaments were dispersed in a liquid and free to rotate or deform in the horizontal plane. If we adapt the boundary condition (15) to the case of two free ends, we obtain

$$\left(\frac{d\phi}{d\Lambda}\right)_{\lambda=0}=\left(\frac{d\phi}{d\Lambda}\right)_{\lambda=\Lambda}=0\Rightarrow\sin^2\phi_0=\sin^2\phi_1$$

with the energetically most stable solution $\phi_0=\phi_1=n\pi, n\in\mathbb{N}$, that is, a straight filament pointing into the field direction. Although the hairpin shape with $\phi_0=\pi-\phi_1=n\pi$ is a solution, too, it is energetically less favorable compared to the straight filament. Nevertheless, hairpin-shaped filaments are frequently observed in Refs. [4] and [8],, which can be attributed to their specific experimental setup. The filaments are first aligned with a static field, which then is rotated quickly by 90°. Whether or not a filament will rotate in its straight form into the new field direction will depend on the ratio of magnetic torque to viscous resistance torque, $M=-\eta F d\phi/dt$, where η is the dynamic viscosity of the surrounding liquid and F the hydrodynamic resistance factor, which for a long slender body scales with L^3 [18]. Short enough filaments obviously can rotate fast enough. Longer filaments, on the other hand, respond to a magnetic torque with bending into a hairpin, thereby halving the hydrodynamically effective length. A thorough analysis of the dynamics of magnetic filaments is given by Refs. [7] and [8].

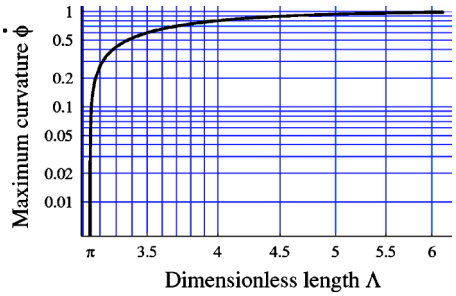

FIG. 7. Maximum dimensionless curvature $\dot{\phi}_{\max}$ of the hairpin shape as a function of the dimensionless filament length Λ on a log-log scale. The hairpin shape can develop for $\Lambda>\pi$ and becomes tighter with increasing Λ. The asymptotic value of the curvature is 1.

The maximum curvature of the hairpin shape,

$$\dot{\phi}_{\max}=\left(\frac{d\phi}{d\lambda}\right)_{\lambda=\Lambda/2} \tag{23}$$

at $\lambda=\Lambda/2$, is of experimental interest and is plotted in Fig. 7 as a function of the dimensionless filament length. For long enough filaments ($\Lambda\gtrsim 5$), $\dot{\phi}_{\max}\approx 1$, or, expressed in absolute units,

$$L\gtrsim 5l_0:\left(\frac{d\phi}{dl}\right)_{l=L/2}=\frac{1}{l_0}=H\sqrt{\frac{4\pi\chi^3 S}{(1+4\pi\chi)E*I}}. \tag{24}$$

It is interesting to compare (24) with Eq. (2) from Ref. [4], who in their derivation neglected the demagnetization factor of the chain of SP particles and therefore obtained an expression linear in χH in the limit case of very long filaments. For values of $\chi\ll 1$, their formula leads to an overestimation of bending rigidity by a factor of $1/(4\pi\chi)$. Because the numerical value of χ was not mentioned in Ref. [4], we are not able to tell whether or not that discrepancy has consequences on the experimental values determined.

It is noteworthy that a shape similar to the hairpin has also been obtained for a pair of ferrogel rods, aligned parallel to each other in zero field, and fixed at their base [11]: in a perpendicular magnetic field of increasing strength, the tips of the rods become more and more deflected toward each other until the slit between the rods shuts. When the field is reduced, the tips straighten out and the pair of rods becomes "permeable" again. This way, a magnetoelastic valve can be realized [11].

D. Bending of fiber with magnetic tip in the vertical plane

So far we have concerned ourselves with magnetic fields applied in the horizontal plane. Now we allow bending to occur in the vertical plane, be it caused by an inclined magnetic field or simply by the uncompensated gravitational force due to the excess mass at the tip. We assume that the mass of the pure fiber can be neglected against the excess mass m of the magnetic material at the tip. The mass m will give rise to a point force at the free end, resulting in a constant line force along the fiber [19]. The total energy of the fiber can now be written as

$$W_{\mathrm{tot}} = W_{\mathrm{SP}}^{0} \sin^2(I-\psi_1) + \int_0^L \left[\frac{EI}{2}\left(\frac{d\psi}{dl}\right)^2 - mg\sin\psi \right] dl \tag{25}$$

where I is the inclination angle of the magnetic field (dip angle with respect to the horizontal); its declination D is assumed to be zero. The vertical z is defined by the gravity vector **g**. It is convenient to express Eq. (25) in a dimensionless form,

$$\omega_{\mathrm{tot}} = \sin^2(I-\psi_1) + \int_0^{\Lambda} \left[\frac{1}{2}\left(\frac{d\psi}{d\lambda}\right)^2 - \alpha\sin\psi \right] d\lambda, \tag{26}$$

where $\Lambda = L/l_0^{\mathrm{SP}}$, with the characteristic length scale l_0^{SP} as defined in Eq. (5), and the gravitational coupling parameter α is given as the ratio of the characteristic gravitational energy of the magnetic tip to its characteristic magnetic energy,

$$\alpha = \frac{c\Delta\rho g l_0^{\mathrm{SP}}(1+4\pi\chi)}{2\pi\chi^3 H^2}, \tag{27}$$

where c is the volume concentration of magnetic material and $\Delta\rho$ the density difference with respect to the surrounding elastic material.

Variation of Eq. (26) delivers the Euler equation

$$\frac{d^2\psi}{d\lambda^2} + \alpha\cos\psi = 0, \tag{28}$$

where

$$\left(\frac{d\psi}{d\lambda}\right)^2 + 2\alpha\sin\psi = C. \tag{29}$$

The second-order nonlinear differential equation (28) is that of a mathematical pendulum (see Ref. [20], p. 700). The integration variable C in our case can be found from the boundary conditions

$$\psi(0) = \psi_0 \quad \text{and} \quad \left(\frac{d\psi}{d\lambda}\right)_{\lambda=\Lambda} = \sin 2(I-\psi_1), \tag{30}$$

as

$$C = \sin^2[2(I-\psi_1)] + 2\alpha\sin\psi_1. \tag{31}$$

The SD case can easily be derived by analogy with

$$\left(\frac{d\psi}{d\lambda}\right)_{\lambda=\Lambda} = \sin(I-\psi_1).$$

Integration of Eq. (28) by separation of variables leads to the following expression:

$$\lambda(\psi) = \int_{\psi_0}^{\psi} \frac{d\tilde{\psi}}{\sqrt{C - 2\alpha\sin\tilde{\psi}}} = 2\int_{\psi_0}^{\psi} \frac{d\tilde{\psi}/2}{\sqrt{(C-2\alpha) + 4\alpha\sin^2(\pi/4 - \tilde{\psi}/2)}}. \tag{32}$$

We now must distinguish three cases.

1. $2\alpha < C \leqslant 2\alpha + 1$

The case $C > 2\alpha$ is relevant when the magnetic field is strong compared to gravity (small α); thus, this case is similar to Sec. II A and equilibrium shapes may be calculated from Eq. (9) to a good approximation. For the sake of completeness, we derive the exact expressions below. Under the condition $C > 2\alpha$, the integration of Eq. (32) leads to

$$\lambda(\psi) = \frac{2}{\sqrt{C-2\alpha}}\left[F\left(\frac{\pi}{4} - \frac{\psi_0}{2}, m\right) - F\left(\frac{\pi}{4} - \frac{\psi}{2}, m\right)\right], \tag{33}$$

where $m = 4\alpha/(2\alpha - C) < 0$. From inverting Eq. (33), we obtain

$$\psi = \frac{\pi}{2} - 2\arcsin\left\{ \mathrm{sn}\left[F\left(\frac{\pi}{4} - \frac{\psi_0}{2}, m\right) - \frac{\sqrt{C-2\alpha}}{2}\lambda \middle| m \right] \right\}. \tag{34}$$

Using the constraint of constant length, the unknown ψ_1 can be determined by numerically solving Eq. (33) with $\lambda(\psi = \psi_1) = \Lambda$. The shape of the fiber may be calculated using Eq. (A3) in the Appendix.

2. $C = 2\alpha$

From Eq. (32) we see that $C = 2\alpha$ is the limit case for long rods, with the solution $\psi_1 = \pi/2$.

3. $C < 2\alpha$

The case $C < 2\alpha$ is relevant for scenarios with large α, that is, if the magnetic field is weak compared to gravity. We let $\sin^2 u_p = (C+2\alpha)/4\alpha$ and rewrite Eq. (32) as

$$\lambda(\psi) = \frac{2}{\sqrt{C+2\alpha}} \int_{u(\psi_0)}^{u(\psi)} \frac{du}{\sqrt{1 - \sin^2 u/\sin^2 u_p}} \tag{35}$$

with $u(\tilde{\psi}) = \tilde{\psi}/2 + \pi/4$, and Eq. (35) can be integrated by analogy to Eqs. (18) and (19); thus

$$\lambda(u) = \frac{1}{\sqrt{\alpha}}\left[F\left(\arcsin\frac{\sin u_{\psi}}{\sin u_p}, \sin^2 u_p\right) - F\left(\arcsin\frac{\sin u_0}{\sin u_p}, \sin^2 u_p\right)\right], \tag{36}$$

so that we finally get

$$\psi = -\frac{\pi}{2} + 2\arcsin\left\{ \sin u_p \times \mathrm{sn}\left[F\left(\arcsin\frac{\sin(\psi_0/2 + \pi/4)}{\sin u_p}, \sin^2 u_p\right) + \sqrt{\alpha}\lambda \middle| \sin^2 u_p \right]\right\}. \tag{37}$$

To find equilibrium states numerically, it is convenient to rewrite the energy functional (26). From Eq. (31), we get

$$\omega = \int_0^{\Lambda} \left[\frac{C}{2} - 2\alpha \sin \psi(\lambda) \right] d\lambda + \sin^2(I - \psi_1) \qquad (38)$$

and have

$$\omega = -\frac{C\Lambda}{2} + \int_{\psi_0}^{\arcsin(C/2\alpha)} \sqrt{C - 2\alpha \sin \psi} d\psi + \int_{\psi_1}^{\arcsin(C/2\alpha)} \sqrt{C - 2\alpha \sin \psi}\, d\psi + \sin^2(I - \psi_1). \qquad (39)$$

Equation (39) is equivalent to Eq. (26) as can be shown by minimizing Eq. (39) with respect to C, which yields exactly Eq. (31).

We will now consider a scenario where the magnetic field is horizontal ($I=0$) and so counteracts gravity ($\alpha=0.5$) by further stabilizing the horizontal initial state. The energy minima here correspond to equilibrium shapes which all have an inflection point (Fig. 8, left) and therefore relatively low bending energy. The same is true for the scenario $I=\pi/4$ (Fig. 8, right). Table I shows that C converges toward 2α for greater values of Λ, which reflects the increasingly dominant role gravity has in controlling the shape of long filaments. The bell-shaped curves in Fig. 8, which represent the case $C<2\alpha$, are energetically more favorable than the corresponding arclike shapes from the scenario $C>2\alpha$, which minimize gravitational energy at the expense of bending energy (see Table I). That advantage, however, declines as Λ increases, because of the growing influence of gravity on longer rods. For $\Lambda \gtrsim 10$ ($I=0, \alpha=0.5$), the minima on the $C>2\alpha$ branch reach the $C=\alpha$ limit, and the corresponding arcs are nearly as energetically favorable as the bell shapes from the $C<2\alpha$ branch. The positions of the minima on the $C>2\alpha$ branch are complementary to the ones on the $C<2\alpha$ branch in such a way that

$$2\alpha - C_{\min(C<2\alpha)} = C_{\min(C>2\alpha)} - 2\alpha.$$

It can also be seen in Fig. 8 and Table I that the alignment of the tip with the magnetic field axis is generally poor for $\alpha=0.5$. When investigating the field dependence of the equilibrium shape of a rod of given length L, one has to bear in mind that $\Lambda \propto H_0^2$ and $\alpha \propto 1/H_0^4$ [see Eqs. (5) and (27)]. Thus, in the limit of strong magnetic fields, the influence of gravity on the equilibrium shape can be neglected, that is, Eq. (9) from the first section can be used to calculate the equilibrium shapes.

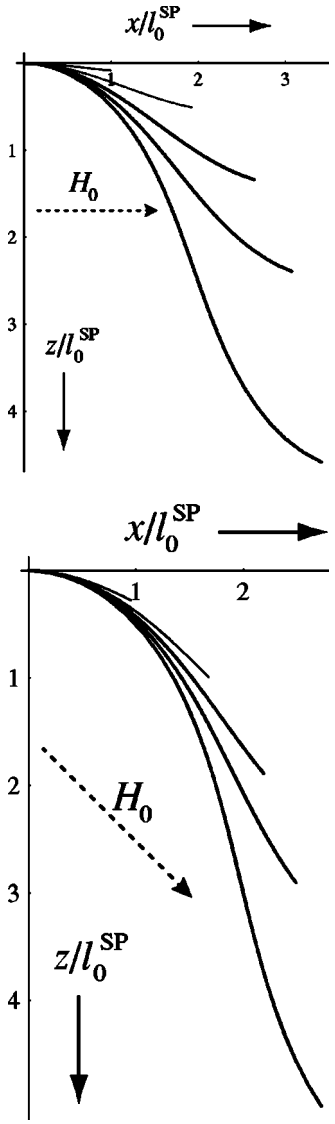

FIG. 8. Equilibrium shape $z(x)$ for several values of $\Lambda \in \{1,2,3,4,6\}$, with $\alpha=0.5$ (case $C<2\alpha$), for $I=0$ (left) and $I=\pi/4$ (right). The magnetic field vector is indicated by the stippled line. The values of C were found from minimizing Eq. (39), the corresponding shapes were computed using Eqs. (37) and (A2). The angle of deflection ψ at the inflection point is $\arcsin(C/2\alpha)$. Note that the tips are not well aligned with the magnetic field axis (except for $\Lambda=2$, $I=\pi/4$), which is due to gravity dominating over the magnetic field. The corresponding values of C, ψ_1, and energy are listed in Table I.

III. CONCLUSIONS

Our mathematical analysis of the magnetoelastic response of magnetic filaments to a static field has shown that there exists a wealth of possible equilibrium shapes. While filaments with a magnetic tip curve into circular arcs when bending is constrained in the horizontal plane, bell-shaped curves are the prevailing equilibrium shapes when bending is allowed to occur in the vertical plane. In the case of strong magnetic fields, however, circular arcs will develop in the vertical plane, just as in the case of bending in the horizontal plane. We also reconsidered the case of filaments with magnetic material distributed over the whole length of the filament. Our analysis here yielded multiform metastable equilibrium states, most of which have been observed in experiments on filaments consisting of superparamagnetic particles held together by molecular linkers. This good agreement with the recently conducted experiments by Refs. [4] and [8], confirms the feasibility of our approach based on continuum mechanics. Our mathematical framework can also be applied to one-dimensional ferrogels and magnetostrictive elastomers. Ferrogels are polymer gels that contain dispersed

TABLE I. Values of C, ψ_1, total energy ω_{tot}, with contributions from magnetic energy ω_{magn}, bending energy ω_{bend}, and gravitational energy ω_{grav} for the equilibrium shapes depicted in Fig. 8 with $\alpha=0.5$, $\psi_0=0$. For comparison, some complementary (metastable) equilibrium states on the $C>2\alpha$ branch are juxtaposed.

I	Λ	C	ψ_1	ω_{tot}	ω_{magn}	ω_{bend}	ω_{grav}
$I=0$							
	1	0.111	0.084	−0.021	0.007	0.014	−0.042
	2	0.340	0.196	−0.131	0.038	0.086	−0.254
	3	0.593	0.293	−0.365	0.083	0.220	−0.669
	3	1.485[a]	2.517	0.284	0.343	1.085	−1.143
	4	0.780	0.358	−0.712	0.122	0.362	−1.197
	6	0.944	0.414	−1.591	0.161	0.540	−2.293
	6	1.055[a]	2.690	−1.511	0.191	0.732	−2.434
	10	0.997	0.432	−3.554	0.175	0.627	−4.356
	10	1.003[a]	2.708	−3.548	0.177	0.656	−4.371
$I=\pi/4$							
≈ 0.785	1	0.526	0.483	0.077	0.089	0.125	−0.138
	2	0.706	0.785	−0.283	0.000	0.212	−0.495
	3	0.811	0.884	−0.662	0.010	0.272	−0.944
	4	0.895	0.937	−1.090	0.023	0.339	−1.452
	6	0.973	0.979	−2.032	0.037	0.424	−2.494

[a]Minimum on branch $C>2\alpha$.

magnetic particles and show magnetic field sensitivity [21]. Such systems are increasingly attracting attention in the design of smart materials [22] and it has been demonstrated that a pair of ferrogel rods can be used as a magnetoelastic valve [11].

An interesting potential application of filaments with magnetic tips is in scanning probe microscopes. A comparatively weak magnetic tip is already sufficient to deflect such a highly flexible fiber. This way, the magnetization structure of the object to be investigated would not be influenced by the probe. Thus, for the examination of magnetically soft materials, probes in the form of magnetic filaments would hold advantages over strong magnetic tips usually employed in magnetic force microscopes (MFM's). By including magnetic gradient forces due to (inhomogeneous) stray fields from the sample, our mathematical formalism can be tailored to the MFM scenario. Lastly, we will employ our model to make quantitative predictions for the working mechanism of the putative magnetic-sense organ of homing pigeons, that is, nerve terminals that each contain some 10–20 clusters of SP magnetite, arranged in a chainlike disposition at the distal end of the dendrite [23]. This will be reported elsewhere [24].

ACKNOWLEDGMENT

We gratefully acknowledge funding from the Deutscher Akademischer Austauschdient (V.S.).

APPENDIX: EQUILIBRIUM SHAPES

1. Magnetic material distributed over filament (Sec. II C)

The expressions for the equilibrium shapes are calculated from

$$\frac{x(l)}{\lambda_0}=\int_0^{\lambda}\cos\psi(\tilde{\lambda})d\tilde{\lambda}=\cos D\int_0^{\lambda}\cos\phi(\tilde{\lambda})d\tilde{\lambda}+\sin D\int_0^{\lambda}\sin\phi(\tilde{\lambda})d\tilde{\lambda},$$

$$\frac{y(l)}{\lambda_0}=\int_0^{\lambda}\sin\psi(\tilde{\lambda})d\tilde{\lambda}=\sin D\int_0^{\lambda}\cos\phi(\tilde{\lambda})d\tilde{\lambda}-\cos D\int_0^{\lambda}\sin\phi(\tilde{\lambda})d\tilde{\lambda}, \tag{A1}$$

with

$$\int_0^{\lambda}\sin\phi(\tilde{\lambda})d\tilde{\lambda}=\int_{\phi_0}^{\phi(\lambda)}\frac{\sin\phi\,d\phi}{\sqrt{\sin^2\phi-\sin^2\phi_1}}=\arcsin\frac{\cos\phi(\lambda)}{\cos\phi_1}-\arcsin\frac{\cos\phi_0}{\cos\phi_1}$$

and

$$\int_0^{\lambda}\cos\phi(\tilde{\lambda})d\tilde{\lambda}=\int_{\phi_0}^{\phi(\lambda)}\frac{\cos\phi\,d\phi}{\sqrt{\sin^2\phi-\sin^2\phi_1}}=\ln\left(\frac{\sin\phi_0+\sqrt{\sin^2\phi_0-\sin^2\phi_1}}{\sin\phi(\lambda)+\sqrt{\sin^2\phi(\lambda)-\sin^2\phi_1}}\right).$$

2. Magnetic material at the tip, vertical field (Sec. II D)

The equilibrium shape is given by

$$x(\psi) = \int \cos\psi(\lambda)d\lambda = \int_{\psi_0}^{\psi} \frac{\cos\tilde{\psi}\,d\tilde{\psi}}{\sqrt{C - 2\alpha\sin\tilde{\psi}}} \quad \text{and}$$

$$z(\psi) = \int \sin\psi(\lambda)d\lambda = \int_{\psi_0}^{\psi} \frac{\sin\tilde{\psi}\,d\tilde{\psi}}{\sqrt{C - 2\alpha\sin\tilde{\psi}}}. \tag{A2}$$

For $C > 2\alpha$, the integrals above can be expressed as

$$x(\psi) = \frac{1}{\alpha}(\sqrt{C - 2\alpha\sin\psi_0} - \sqrt{C - 2\alpha\sin\psi}), \tag{A3}$$

$$z(\psi) = \frac{\sqrt{C - 2\alpha}}{\alpha}\left[E\left(\frac{\pi}{4} - \frac{\psi}{2}, m\right) - E\left(\frac{\pi}{4} - \frac{\psi_0}{2}, m\right)\right] + \frac{C}{a\sqrt{C - 2\alpha}}\left[F\left(\frac{\pi}{4} - \frac{\psi_0}{2}, m\right) - F\left(\frac{\pi}{4} - \frac{\psi}{2}, m\right)\right],$$

where $m = 4\alpha/(2\alpha - C) < 0$ and E is the incomplete elliptic integral of the second kind,

$$E(\phi, m) = \int_0^{\phi} \sqrt{1 - m\sin^2\beta}\,d\beta.$$

[1] S. Smith, L. Finzi, and C. Bustamante, Science **258**, 1122 (1992).
[2] J. H. Shin, L. Mahadevan, P. So, and P. Matsudaira, J. Mol. Biol. **337**, 255 (2004).
[3] W. Wang, J. P. Butler, and D. E. Ingber, Science **260**, 1124 (1993).
[4] C. Goubault, P. Jop, M. Fermigier, J. Baudry, E. Bertrand, and J. Bibette, Phys. Rev. Lett. **91**, 260802 (2003).
[5] E. M. Furst, C. Suzuki, M. Fermigier, and A. P. Gast, Langmuir **14**, 7334 (1998).
[6] E. M. Furst and A. P. Gast, Phys. Rev. Lett. **82**, 4130 (1999).
[7] A. Cebers, J. Phys.: Condens. Matter **15**, S1335 (2003).
[8] A. Cebers and I. Javaitis, Phys. Rev. E **69**, 021404 (2004).
[9] R. P. Blakemore, Science **19**, 377 (1975).
[10] V. P. Shcherbakov, M. Winklhofer, M. Hanzlik, and N. Petersen, Eur. Biophys. J. **26**, 319 (1997).
[11] P. Voltairas, D. Fotiadis, and C. V. Massalas, J. Appl. Phys. **93**, 3652 (2003).
[12] D. Steigmann, Int. J. Non-Linear Mech. **39**, 1193 (2004).
[13] V. Naletova, V. Turkov, Y. Shkel, and D. Klingenberg, J. Magn. Magn. Mater. **202**, 570 (1999).
[14] L. C. Davis, J. Appl. Phys. **85**, 3348 (1999).
[15] V. Turkov, J. Magn. Magn. Mater. **252**, 156 (2002).
[16] L. D. Landau and E. M. Lifschitz, Phys. Z. Sowjetunion **8**, 153 (1935).
[17] *Handbook of Mathematical Functions*, Natl. Bur. Stand. (U.S.) Appl. Math. Ser. No. 55, edited by M. Abramowitz and I. Stegun (U.S. GPO, Washington, D.C., 1969).
[18] S.-M. Yang and L. Leal, J. Fluid Mech. **136**, 393 (1983).
[19] L. D. Landau and E. M. Lifschitz, *Elastizitätstheorie*, Lehrbuch der Theoretischen Physik Vol. 7 (Akademie-Verlag, Berlin, 1970).
[20] I. Bronshtein, K. Semendyayev, G. Musiol, and H. Muehlig, *Handbook of Mathematics*, 4th ed. (Springer, Berlin, 2004).
[21] M. Zrínyi, L. Barsi, and A. Büki, J. Chem. Phys. **104**, 8750 (1996).
[22] Z. Varga, J. Fehér, G. Filipcsei, and M. Zrínyi, Macromol. Symp. **200**, 93 (2003).
[23] G. Fleissner, E. Holtkamp-Rötzler, M. Hanzlik, M. Winklhofer, G. Fleissner, N. Petersen, and W. Wiltschko, J. Comp. Neurol. **458**, 350 (2003).
[24] A. F. Davila, M. Winklhofer, V. P. Shcherbakov, and N. Petersen (unpublished).